Study of rotational ground motion in the near field region

Marco STUPAZZINI[1], Josep DE LA PUENTE[2], Chiara SMERZINI[1],
Martin KÄSER[2], Heiner IGEL[2], Alberto CASTELLANI[1]

Corresponding Author:
Marco STUPAZZINI
Department of Structural Engineering
Politecnico di Milano
P.zza Leonardo da Vinci, 32
20133 Milano, Italy
Mail : stupa@stru.polimi.it
Tel: +39 02 2399 4317
Fax: +39 02 2399 4220
Web: http://www.stru.polimi.it

ABSTRACT

While the earthquake induced translational wave field has been recorded and studied since the nineteenth century, the rotational motion still nowadays remains poorly observed and investigated. We aim at further understanding the rotational ground motion and its relation to the translational wave field with a special emphasis on the near field, few wavelengths away from the hypocenter, where damage related to rotational motion might need to be considered. A broad picture of the available values of rotational amplitudes and their variability is obtained by gathering most of the published data on strong rotational motion. To obtain a more detailed picture, we perform a large scale 3D numerical study of a strike-slip event in the Grenoble valley, where a combination of topographic, source, and site effects produces a realistic wave field. The size of the synthetic dataset allows us to study the distribution of the rotational and translational peak amplitudes and their dependence on two effects: non-linear soil behaviour and source directivity. Finally, we compare our numerical results in terms of Peak Ground Velocity, *PGV*, vs. Peak Ground Rotation, $PG\omega$, with field data obtained at similar scenarios (e.g. Parkfield) by array techniques to investigate the relation between translational and rotational amplitudes which can be expected in the near-field for shallow medium-sized earthquakes. Furthermore, the spatial variations of $PGV / PG\omega$ ratio show a trend that seems to be correlated with the velocity structure of the model under study.

Introduction

Earthquakes radiate large amounts of energy, mostly as seismic waves. Classically, seismologists recorded through different devices, seismometers or accelerometers, only the three degrees of freedom associated with the translational motion (i.e. velocity, $\underline{\dot{u}} = \left[\dot{u}_x, \dot{u}_y, \dot{u}_z\right]$), or acceleration along a Cartesian reference frame, implicitly neglecting the rotational components of the motion. Nevertheless, the investigation of the latter cannot be obviated a priori in risk assessment studies, as it has already been acknowledged that rotational ground motion plays a role in the dynamic response or damage induced by certain earthquakes on buildings (Richter 1958, Newmark 1969, Stratta and Griswold 1976, Kalkan and Graizer 2007).

A direct observation of earthquake-induced rotational ground motion is possible using devices sensitive to torsion as tilt meters or, more recently, solid state devices (Nigbor 1994) and ring lasers (Stedman et al. 1995). However, such devices are not in common use and most frequently the rotational components of motion are indirectly estimated from array measurements (e.g. Spudich et al. 1995, Huang 2003, Suryanto et al. 2006, Ghayamghamian and Nouri 2007, Spudich 2008). The records of translational and rotational components of motion have been proved to be useful, for example, in the extraction of local phase velocities or the back-azimuth of events (Igel et al. 2005; 2007) or in recovering the static displacement (Trifunac and Todorovska 2001, Graizer 2005, Graizer 2006, Pillet & Virieux 2007). Regardless the recent interest in the field, studies of recorded rotational ground motion, for teleseismic or local events, are still rare and our knowledge of the rotational wave field is largely insufficient.

In spite of the lack of observed data, numerical studies have been performed aiming at computing synthetic time histories in order to investigate the influence of important factors on the rotational motion and, in particular, their expected maximum amplitudes. A pioneering numerical study was accomplished by Bouchon & Aki (1982) and further numerical experiments have followed (Lee and Trifunac 1987, Takeo 1998, Wang et al., 2008). In our case, we simulate several events in a 3D model of an Alpine valley at Grenoble, France, with an alluvium filled basin so that topographic, soil and source effects can be all considered. The synthetic results are compared with data retrieved mainly from array experiments, and investigated in terms of the following ratio as already done by Wang et al. (2008) and Fichtner et al. (2008):

$$\frac{PGV_h(\underline{x})}{PG\omega_z(\underline{x})} \approx 2c_s\,, \tag{1}$$

where $PGV_h(\underline{x})$ is the maximum value in time of $\sqrt{\dot{u}_x^2 + \dot{u}_y^2}$ at location $\underline{x}$, $PG\omega_z(\underline{x})$ is the peak ground vertical rotation and c_s can be regarded as a scaling factor between translational and rotational peak ground motion. Investigating the correlation of this ratio with the local velocity allows us to address the question of whether we can obtain reliable peak rotational motion estimates straight from translational motion studies.

The paper is structured as follows. First, we give an overview on studies related to rotational ground motion recordings, both observational and numerical, and the general trends and characteristics observed in them. In the next section, we introduce and validate a 3D method to simulate the translational and rotational ground motion produced in complex scenarios. A particular case study follows, where we simulate a M_W = 6.0 strike-slip earthquake occurring in the Grenoble

valley. Moreover, we compare the rotational wave field both at the bedrock and the sedimentary basin and we draw peak ground motion maps for different magnitudes, sediment mechanical properties and source hypocenter locations. Finally, we put our synthetic dataset in direct comparison with past simulations and observations in terms of the ratio given by Eq. (1) to draw conclusions about the correlation between translational and rotational ground motion and its physical implications.

Past studies in rotational seismology

In the last decades few studies have shown direct measurements of rotations, thus leading to large uncertainties in the order of magnitudes of rotations likely to occur for a given earthquake scenario. Therefore, it is important to synthesize in a comprehensive way a selection of the data available in the literature. Specifically, we chose data which might be of relevance for seismic engineering studies, namely those recorded in the near field (few wavelengths away from the epicenter) or showing relatively strong rotation amplitudes, even if recorded at greater distance.

For sake of completeness, we combine field data records with synthetic studies, observations at stiff and soft soils, array-derived with single-point measurements and those generated by different source mechanisms. A proper labeling helps subdividing them into groups which can be directly compared to each other. In the following, we present briefly the sources of data that we use and which are listed in Table I.

A pioneering work was published by Bouchon & Aki (1982), who adopted a semi-analytical method to derive strains, tilts and rotations in the proximity of a buried 30 km long strike slip fault with seismic moment 8×10^{18} Nm, obtaining a peak ground rotation of the order of $3\ 10^{-4}$ rad while the corresponding rotational rate was about $1.5\ 10^{-3}$ rad/sec. Later on, different analyses have tried to record and characterize ground rotational motions. Most of these studies are based on indirect estimates of surface ground rotations from two-dimensional seismic arrays (see e.g. Castellani & Boffi, 1986; Oliveira & Bolt, 1989; Bodin et al., 1997; Singh et al, 1997; Huang, 2003; Spudich & Fletcher, 2008). The most significant drawback of such an approach is the limited frequency content (typically lower than 2 Hz), due to the relatively large separation distance between adjacent receivers. Besides field observations, ground rotations have been also investigated from a theoretical point of view. Those studies rely either on the theory of elastodynamics for plane wave propagation in ideal media (Trifunac, 1982; Lee and Trifunac, 1985) or on kinematic source models

(Takeo & Ito, 1997). The direct measurement of rotations has been obtained at great distances from important earthquakes using ring laser instruments (McLeod et al., 1998; Pancha et al., 2000; Cochard et al., 2006; Igel et al., 2005 and 2007) and in the near field through triaxial rotational sensors (Nigbor 1994; Takeo, 1998). In particular, Nigbor measured an explosive source, whereas Takeo recorded an earthquake swarm in 1997, offshore the city of Ito in Japan. The two largest events of that swarm have seismic moments of 1.2 10^{17} Nm and 2.7 10^{16} Nm and were recorded at 3.3 km from the fault. The maximum measured rotational rates around the vertical axis were, respectively, 3.3 10^{-3} rad/s and 8.1 10^{-3} rad/s, several times higher than what was predicted by Bouchon and Aki (1982), even though the seismic moment of the two events was about two orders of magnitude smaller than the one simulated by the authors. This discrepancy cannot be explained as a malfunction or limited sensitivity of the instruments, therefore the author claimed that the large rotational velocities might be induced by either the heterogeneity of slip velocity along the fault or the local rheology. These two factors may play a crucial role, particularly in the near field, as was stressed by Huang (2003) and Spudich & Fletcher (2008).

Table I – List of selected literature data, mainly recorded in the near field (few wavelengths away from the epicenter) or showing relatively strong rotation amplitudes even if recorded at greater distance. Peak values of horizontal ground velocity (PGV_h), vertical ground rotation ($PG\omega_z$) and rotational velocity ($PG\dot{\omega}_z$) about the vertical axis. Additional information concerning the data type, the source parameters (magnitude, epicentral distance R and source mechanism) and type of soil (a simplified classification was assumed between soft and stiff soil).

Reference	**#**	**Data type**	**EQ. parameters**			**Type of soil**	PGV_h **[m/s]**	$PG\omega_z$ **[rad]**	$PG\dot{\omega}_z$ **[rad/s]**	**Symbol**
			M_w	***R* [km]**	**Source mech.**					
Bouchon & Aki (1982)	1	2	6.6	1	SS	1	1	2 10^{-4}	1.2 10^{-3}	▼
	2		6.6	1	SS	1	1.6	3 10^{-4}	1.5 10^{-3}	▼
Lee & Trifunac (1985)	3	2	6.6	10	N.A.	1	0.45	1 10^{-4}	1.2 10^{-3}	▼
Niazi (1986)	4	1	6.6	5	SS	2	0.203	2.75 10^{-4}	7 10^{-4}	△
Oliviera &	5	1	5.6	6	N.A.	1	0.15	7.4 10^{-6}	N.A	▲

Bolt (1989)	6		5.7	30	N.A	1	0.12	$8.5\ 10^{-6}$	N.A	▲
	7		5.8	22	N.A	1	0.30	$1.46\ 10^{-5}$	N.A	▲
	8		6.7	84	N.A	1	0.06	$6.8\ 10^{-6}$	N.A	▲
	9		7.8	79	N.A	1	0.391	$3.93\ 10^{-5}$	N.A	▲
Castellani & Boffi (1989)	10	2	6.6	18	SS	1	0.0692[3]	$3.06\ 10^{-5}$	$1.04\ 10^{-4}$	▼
Nigbor (1994)	11	3	1 kton	1	*Expl.*	1	0.2780	$6.6\ 10^{-4}$	$2.4\ 10^{-2}$	×
Bodin et al.; Singh et al. (1997)	12	1	6.7	311	R	2	0.03	$5.6\ 10^{-5}$	N.A	△
	13		7.5	305	R	2	0.11	$2.07\ 10^{-4}$	N.A	△
Takeo (1998)	14	3	5.7	3.3	SS	1	0.29	N.A.	$3.3\ 10^{-3}$	×
	15	3	5.3	3.3	SS	1	0.20	N.A.	$8.1\ 10^{-3}$	×
Huang (2003)	16	1	7.7	6	T	1	0.33	$1.71\ 10^{-4}$	N.A	▲
Data retrieved with the methodology illustrated in Paolucci & Smerzini (2008)	17	1	4.2	81	?	2	$4.06\ 10^{-4}$	*Mean* $1.64\ 10^{-7}$ *Min* $8.79\ 10^{-8}$ *Max* $3.38\ 10^{-7}$	$2.4\ 10^{-4}$ $1.75\ 10^{-4}$ $4.7\ 10^{-4}$	⊖
	18		4.9	81	?	2	$5.2\ 10^{-3}$	*Mean* $2.25\ 10^{-6}$ *Min* $1.16\ 10^{-6}$ *Max* $3.33\ 10^{-6}$	$3.2\ 10^{-3}$ $1.8\ 10^{-3}$ $5.0\ 10^{-3}$	⊖
	19	1	6.0	11.6	SS	1	0.25	*Mean* $8.98\ 10^{-5}$ *Min* $4.07\ 10^{-5}$ *Max* $1.51\ 10^{-4}$	$1.3\ 10^{-3}$ $3.5\ 10^{-4}$ $1.6\ 10^{-3}$	●
	20		6.5	65	SS	1	0.165	*Mean* $7.68\ 10^{-5}$ *Min* $4.23\ 10^{-5}$ *Max* $1.25\ 10^{-4}$	$8.2\ 10^{-4}$ $2.8\ 10^{-4}$ $1.6\ 10^{-3}$	●
Spudich & Fletcher (2008)	21	1	6.0	8.8	SS	1	0.25 0.20 0.28 0.27	*Broad Band* $8.81\ 10^{-5}$ *Array1-3* 2.25E-05 *Array8-11* 6.17E-05 *Array5-12* 3.56E-05	$1.09\ 10^{-3}$ $1.39\ 10^{-4}$ $4.48\ 10^{-4}$ $2.23\ 10^{-4}$	◬
	22		4.7	14.0	SS	1	$1.19\ 10^{-2}$ $1.27\ 10^{-2}$ $9.16\ 10^{-2}$ $1.19\ 10^{-2}$	*Broad Band* $4.69\ 10^{-6}$ *Array1-3* $1.64\ 10^{-6}$ *Array8-11* $1.88\ 10^{-6}$ *Array5-12* $1.43\ 10^{-6}$	$9.44\ 10^{-5}$ $9.12\ 10^{-6}$ $1.08\ 10^{-5}$ $7.47\ 10^{-6}$	◬
	23		5.1	14.4	SS	1	$6.02\ 10^{-2}$	*Broad Band* $2.0\ 10^{-5}$	$4.46\ 10^{-4}$	◬

							4.41 10^{-2}	*Array1-3* 3.48 10^{-6}	2.10 10^{-5}	
							5.96 10^{-2}	*Array8-11* 5.14 10^{-6}	3.22 10^{-5}	
							6.91 10^{-2}	*Array5-12* 4.42 10^{-6}	2.49 10^{-5}	
	24		4.9	18.3	SS	1	2.74 10^{-2}	*Broad Band* 1.36 10^{-5}	2.47 10^{-4}	▲
							2.0 10^{-2}	*Array1-3* 2.73 10^{-6}	1.23 10^{-5}	
							3.0 10^{-2}	*Array8-11* 5.67 10^{-6}	2.69 10^{-5}	
							3.15 10^{-2}	*Array5-12* 3.16 10^{-6}	1.64 10^{-5}	

Legend of Table I

Data type:	**Source Mechanism**	**Soil Type**
1 = array-derived. (▲ or ● for data from #17 to #20) 2 = numerical/semi-analytical (▼) 3 = measured (✕)	SS = strike-slip T = thrust R = reverse	Distinction between soft and stiff soil were based on Vs30: soft if Vs30 < 300 m/s 1 = stiff (black marker face color, e.g.: ▲ or ●) 2 = soft (white marker face color, e.g.: △ or ○)

Numerical method validation

As a complement to the recorded data, we use synthetic rotational seismograms obtained with the Spectral Element Method (SEM), first introduced for the solution of the elastodynamic problems by Priolo and Seriani (1991), Faccioli et al. (1997) and Komatitsch and Vilotte (1998). Here we adopt the version implemented in the software package GeoELSE (Stupazzini et al., 2008). A detailed description can be also found at http://geoelse.stru.polimi.it. In order to validate the reliability of the rotational output produced by our method, we compare our results with those obtained with the highly accurate ADER-DG method (Käser and Dumbser, 2006 and Dumbser and Käser, 2006).

Both methods are, essentially, high-order finite element methods explicit in the time domain, able to accurately model large velocity contrasts, attenuation effects and finite-source kinematics, all of them crucial aspects for reproducing realistic earthquake scenarios in complex geological configurations.

We choose first to cross-validate the synthetics produced by our methods, both translational and rotational, for two established tests proposed by the Southern California Earthquake Center (Day et al., 2007). Those are the so-called LOH.1 and LOH.2 tests, where the acronym LOH stands for

Layer Over Halfspace. Both of them describe a flat half-space, on top of which lies a thin low-velocity layer. The main difference between both tests is that LOH.1 uses a point-source whereas LOH.2 uses a source with finite extent, thus leading to different waveforms and frequency contents. For the translational motion, both methods have already been tested against quasi-analytical solutions (Stupazzini, 2004, Dumbser and Käser, 2006). The setup of the tests and an example of the computational mesh for SEM are depicted in Figure 1. The parameters describing both models are shown in the legend. Besides the translational motion ($\underline{u} = \left[u_x, u_y, u_z\right]$), we output rotational ground motion, which is defined as

$$\omega_x = \frac{1}{2}\left(\frac{\partial u_z}{\partial y} - \frac{\partial u_y}{\partial z}\right), \omega_y = \frac{1}{2}\left(\frac{\partial u_x}{\partial z} - \frac{\partial u_z}{\partial x}\right), \omega_y = \frac{1}{2}\left(\frac{\partial u_y}{\partial x} - \frac{\partial u_x}{\partial y}\right) \tag{2}$$

and their corresponding rotational velocities and accelerations

$$\dot{\omega}_i = \frac{d\omega_i}{dt}, \ \ddot{\omega}_i = \frac{d^2\omega_i}{dt^2} \text{ with } \quad i = x,y,z\,. \tag{3}$$

A comparison of the synthetics obtained with both methods can be found in Figure 2. In this case, the SEM solution has been computed with a mesh of 352,800 hexahedral elements using polynomials of degree 4 to describe the variables while the ADER-DG solution has been computed with polynomials of degree 3 and a mesh with 782,542 tetrahedral elements. The agreement between both methods is remarkable, and only after 7 seconds some major differences arise owing to the spurious reflections coming from the absorbing boundaries. It can be further observed that the ω_z motion is delayed with respect to other signals, as it is only sensitive to SH motion. Similar results characterized the records of all stations.

From these tests we conclude that both methods' solutions are in satisfactory agreement and that they are able to produce reliable translational and rotational synthetic seismograms in three-dimensional setups.

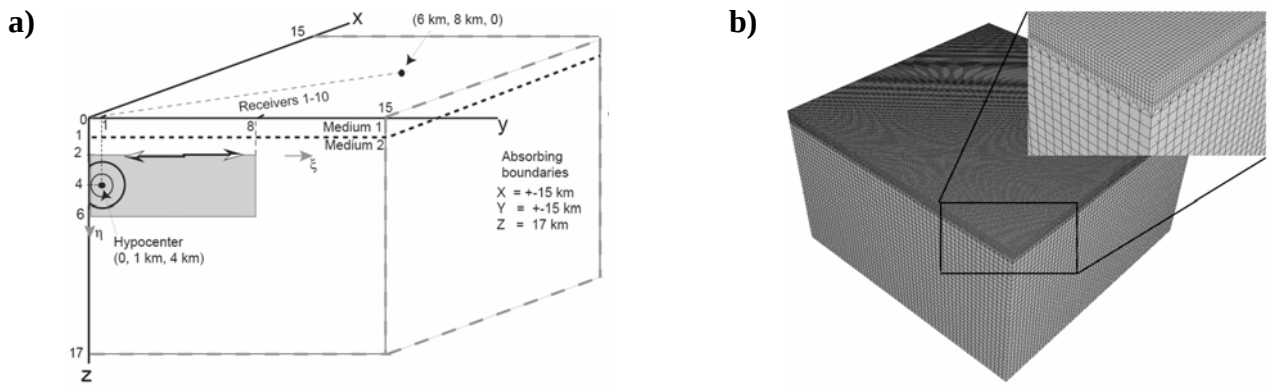

Figure 1. (a) One of four symmetric quarters of the LOH test cases, consisting of a surface layer, 1 km thick (Material 1: ρ= 2600kg/m^3, V_S = 2000m/s, V_P = 4000m/s), overlying a bedrock (Material 2: ρ = 2700 kg/m^3, V_S = 3464 m/s, V_P = 6000 m/s). The hypocenter and rupture surface of case LOH.2 are also shown, together with the receiver locations for the following Figure 2. (b) Spectral element mesh adopted for the LOH.1 and LOH.2 cases. Notice the mesh refinement at the low-velocity layer.

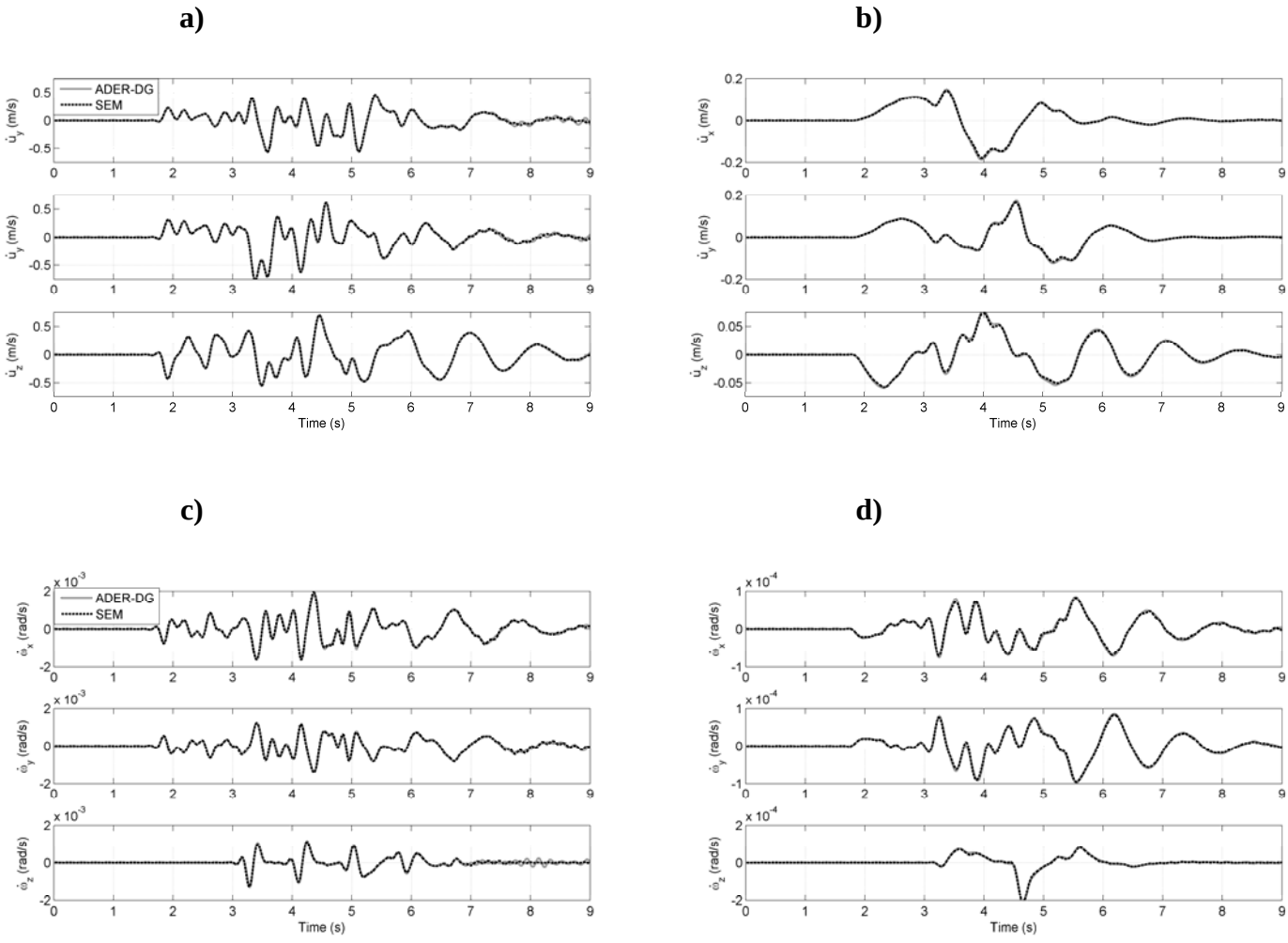

Figure 2. Comparison of the translational (a) and (b) and rotational rate (c) and (d) for the LOH.1(a) and (c) and LOH.2 (b) and (d) test cases at the surface. The receiver coordinates are: (6000, 8000, 0)m. The SEM solution is plotted in black and the ADER-DG solution in grey.

A study case: Grenoble valley (French Alps)

Studies by Bouchon and Aki (1982), Lee and Trifunac (1985) and Castellani and Boffi (1986) indicated that rotational ground motion could be important in the near-field and for surface waves. Although in recent time direct (Nigbor, 1994; Takeo, 1998) and indirect (Graizer, 1989; Huang, 2003) measurements of rotation have received a certain emphasis, still the number of available records is extremely limited and, furthermore, there are only a few examples of data in the near field region (Spudich and Fletcher, 2008). As a consequence, our level of knowledge on the magnitude of rotational ground motions to be expected for a given earthquake scenario is still limited.

In this paper, we make use of 3D numerical modeling to reproduce the rotational wave field generated by strike-slip earthquakes in the near field. We choose as our study area the Grenoble valley (French Alps) for two main reasons. First of all, when it comes to large scale numerical simulations, the validity of the results is hard to assess. As models grow complex, the amount of parameters to be taken into account increases severely and so does the possibility of introducing unexpected errors in the computation. The Grenoble case, in particular, has the great advantage of having been successfully benchmarked by cross-validation between many state-of-the-art simulation techniques (Chaljub 2006), including the SEM and ADER-DG methods used in the previous section. This increases significantly our degree of confidence on the synthetic results. A second but not less important reason is the fact that the Grenoble valley offers the chance to investigate many factors which can be crucial for amplification phenomena in the near field such as site, topographic, and source directivity effects.

The model of the Grenoble valley has been constructed using a 250 m resolution digital elevation model (DEM) of the surrounding topography and of the shape of the basin. The basin's soil is described by the following polynomial variation with depth z (measured in m):

$$V_P = 1450+1.5z, \quad V_S = 300+19z^{1/2}, \quad \rho = 2140+0.125z, \quad Q_S = Q_P = 50 \qquad (4)$$

where V_P and V_S are the P- and S-wave velocities (in m/s), respectively, ρ is the mass density (in kg/m^3), and Q_P and Q_S are P- and S-wave quality factors. The surrounding bedrock is two-layered, with V_P = 5600 m/s and V_S = 3200 m/s, between 0 and 3 km depth, and V_P = 5920 m/s and V_S = 3430 m/s, between 3 and 27 km depth.

In the following, the GeoELSE version of the Spectral Element Method has been used to compute the synthetic seismograms. All the computations were performed with tethys cluster (Oeser et al., 2006). A linear viscoelastic material is used to model the attenuation. The final computational mesh consists of 216,972 elements, the size of which ranges from a minimum of about 20 m inside the alluvial basin up to 900 m at some bedrock areas. The mesh has been designed to propagate frequencies up to 2 Hz with a spectral degree SD = 3, and up to around 3 Hz with SD = 4.

We use the source specification denoted as "Strong motion 1" case by Chaljub (2006) and which corresponds to a M_W = 6.0 earthquake originated at the Eastern segment of the Belledonne Border Fault (see Figure 3a). The fault is defined as a 9 km x 4.5 km rectangle where "in plane" rupture occurs with a uniform slip of 1 m. The mechanism is strike slip, right-lateral (strike = 45°, dip = 90° and rake = 180°). The rupture propagates circularly from the hypocenter, located at the centre of the fault, with velocity v_r = 2.8 km/s. The time history of the seismic moment tensor source is described by an approximate Heaviside function of the type:

$$M_0(t) = \frac{1}{2}\left[1 + erf\left(2.0\frac{t-2\tau}{\tau/2}\right)\right], \tag{5}$$

where *erf* is the error function and τ = 1.116 s is a rise time. These values are selected for the slip velocity to be approximately 1 m/s. A total of 750 spectral nodes are contained in the fault. In the following (see Section "Relationship between translational and rotational peak values") we also refer to a smaller earthquake (M_W=4.5) simulated for the same fault plane. In that case, we use a smaller rectangular fault, measuring 4 km x 3 km, where the total slip has been reduced to a value of 0.02m, leaving the remaining parameters unchanged with respect to the M_W=6.0 event.

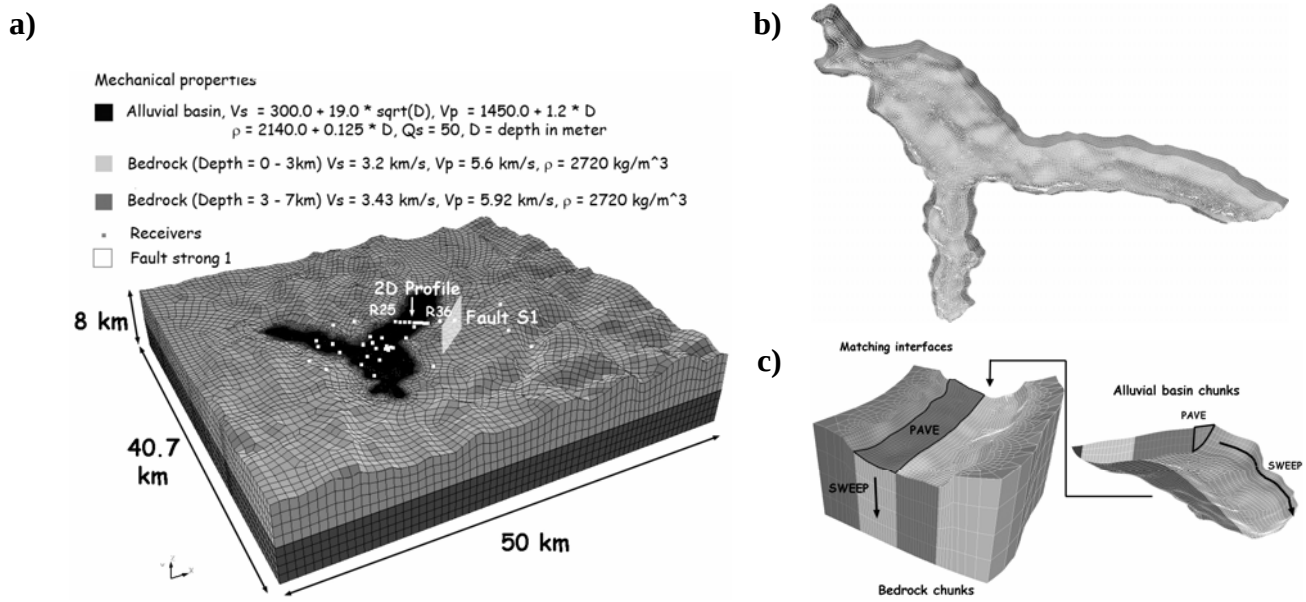

Figure 3 – (a) The 3D hexahedral spectral element mesh used for the computation of the Grenoble scenario with the GeoELSE software package. The computational domain is subdivided into small chunks, each of them is sequentially meshed starting from the alluvial basin down to the bedrock. For simplicity, the spectral elements are shown without the Gauss-Lobatto-Legendre nodes. (b) Detailed view (from the bottom) of the alluvial basin mesh. (c) Mesh adapted to best fit the soft soil-bedrock interface.

Parametric study of near-fault earthquake ground motion in the Grenoble Valley

Our study of the Grenoble M_W=6.0 scenario begins by investigating the effect of various parameters in the rotational and translational motion records. This allows us to discern those parameters which more strongly affect the rotational wave field and get a wider view on the variability of the amplitudes that we can expect. In particular, we record the peak ground motion recorded at a very dense array of synthetic stations inside and near the alluvial basin of Grenoble. Our observables are the peak ground vertical rotation, $PG\omega_z$, and the peak ground horizontal rotation, $PG\omega_h$, defined as the maximum of $|\omega_z|$ and of $\sqrt{\omega_x^2+\omega_y^2}$, respectively. Similarly, we use the peak of their respective time derivatives or "rates" ($PG\dot{\omega}_z$ and $PG\dot{\omega}_h$).

In this contribution two main phenomena are studied: source directivity and the presence of a non-linearly behaving soil at the basin. The source directivity effect for the Grenoble case was studied by Stupazzini et al. (2008) and has here been recomputed, now outputting the rotational motion components. Three different directivity cases are studied: neutral, forward and backward. In

the neutral case the hypocenter is located in the middle of the fault plane (Hypocenter 1), as has been described in last section. The other two consider that the hypocenter is situated very close to the NE or SW tips of the fault (Hypocenters 2 and 3, respectively), while keeping the total slip and the slip rate function unaltered. As a result, all three earthquakes have the same magnitude but their radiation pattern is much larger in the direction directly opposed to their hypocenter position. The exact location of the hypocenters for all three cases can be seen in Figure 4.

The second source of variability of ground motion is the presence of a non-linear vicoelastic soil, instead of the linear viscoelastic one. The non-linear viscoelastic soil model implemented in GeoELSE can be regarded as a generalization to 3D load conditions of the classical G-γ and D-γ curves used within 1D linear-equivalent approaches (e.g. Kramer, 1996), where G, D and γ are shear modulus, damping ratio and 1D shear strain, respectively. Namely, to extend those curves to the 3D case, a scalar measure of shear strain amplitude was considered as:

$$\gamma_{\max}(\underline{x},t) = \max\left[\left|\varepsilon_I(\underline{x},t) - \varepsilon_{II}(\underline{x},t)\right|, \left|\varepsilon_I(\underline{x},t) - \varepsilon_{III}(\underline{x},t)\right|, \left|\varepsilon_{II}(\underline{x},t) - \varepsilon_{III}(\underline{x},t)\right|\right] \quad (6)$$

where ε_I, ε_{II} and ε_{III} are the principal values of the strain tensor. Once the value of γ_{max} is calculated at the generic position $\underline{x}$ and generic time t, this value is introduced in the G-γ and D-γ curves and the corresponding parameters are updated for the following time step. Therefore, unlike the classical linear-equivalent approach, the initial values of the dynamic soil properties are recovered at the end of the excitation. The G-γ and D-γ curves specifically calibrated on the Grenoble shallow soil materials described by Jerram et al. (2006) were adopted in this work (Figure 5).

The results of our parametric study have been plotted in Figure 6 and 7. The first two columns show the peak ground rotational motion with threshold limits of 10^{-5} rad and 10^{-4} rad/s in order to highlight the pattern produced on the outcropping bedrock and the clear amplification inside the alluvial basin. The rest of the columns use non-saturated plots only of the peak ground rotational motion recorded inside the basin and show the combined effects of directivity and linear/non-linear soil descriptions.

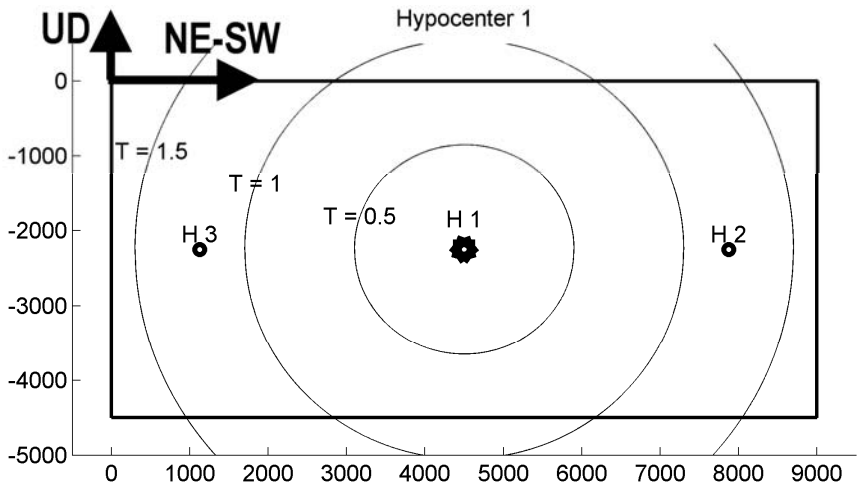

Figure 4. Hypocenter location possibilities. Isochrones of the triggered slip starting from hypocenter 1 are shown as thin lines. The rupture propagates circularly from the selected hypocenter with v_r=2800 m/s.

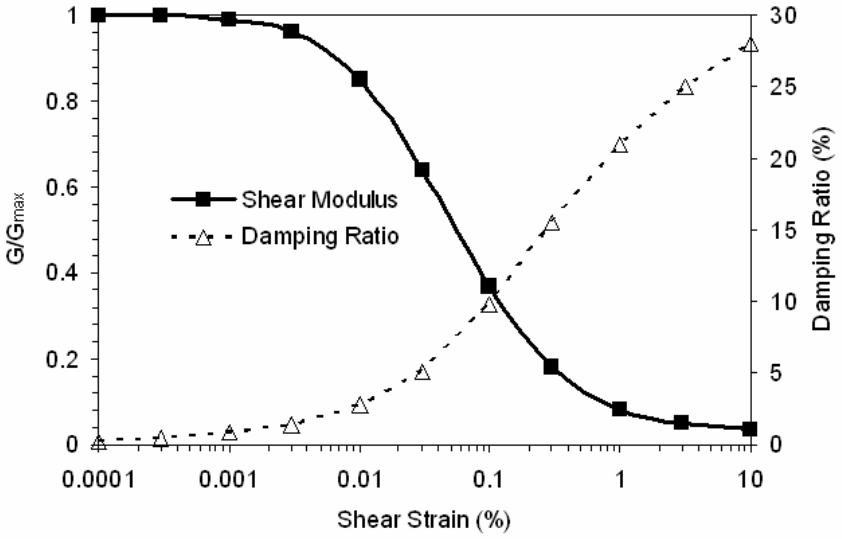

Figure 5 – Curves of normalized shear modulus (G) and damping ratio (D) as a function of shear strain (γ), adopted for the alluvium shallow materials in the Grenoble basin. From Jerram et al., 2006.

As a reference we can take the values obtained for a linear elastic basin with neutral directivity. In this case we observe peak values of $PG\omega_z$=1.69x10^{-3} rad, $PG\omega_h$=1.31x10^{-3} rad for the rotations and $PG\dot{\omega}_z$=8.24x10^{-3} rad/s, $PG\dot{\omega}_h$=8.66x10^{-3} rad/s for the rotation rates, mostly recorded at the southern tip of the Y-shaped basin, owing to the constructive interference between the local sedimentary structure and the radiation pattern. As a general trend, we can observe that the

combination of forward directivity and non-linear elasticity produces the strongest rotational motions whereas the combination of backward directivity and linear elasticity produces the smallest amplitudes.

Another conclusion from our study is that two main potentially dangerous areas can be identified. One of them is the whole southern tip of the basin and the other is the part of the basin located closest to the fault, i.e. its northeastern tip. Peak rotation and rotation rate maxima are consistently recorded at those two areas, particularly at their eastern most sides. This clustering of the maxima towards the edge of the basin is further increased in the presence of non-linear soils. The northwestern tip of the basin, on the other hand, always records values of rotation and rotation rates around five times smaller than the other basin areas.

The observed range of variability, from "worst" to "best" case, for both rotation and rotation rate maxima is of around a factor of 3 for the vertical components and around a factor 6 for the horizontal components. Most of the variation is coming from directivity effects, although the non-linear soil behavior can also play a significant role. Previous fault normal *PGV* studies (Stupazzini et al. 2008) found a similarly strong effect of the directivity on the maximum recorded *PGV* values, which can range from 0.35 m/s for H_3 seismic source up to 2.09 m/s for H_2. As a consequence, both 3D and soil effects produce large spatial variability in the rotational motion which cannot be accounted for using simplified models (i.e.: 2D models or only viscoelastic constitutive behaviour).

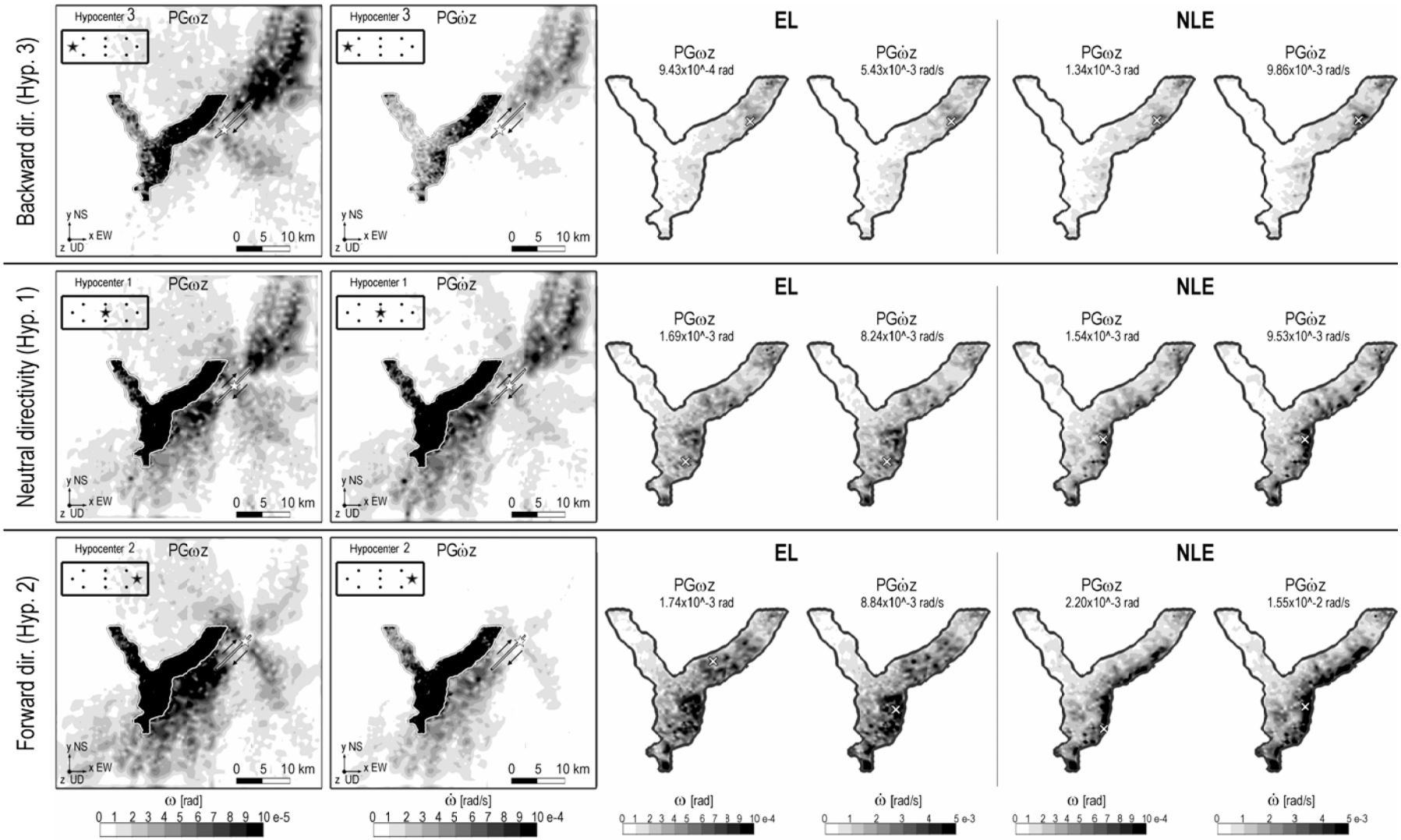

Figure 6. Set of 3D simulations used as parameter study. Maps of $PG\omega_z$ and $PG\dot{\omega}_z$. Six scenarios are considered: backward directivity (Hyp. 3), neutral directivity (Hyp. 1) and forward directivity (Hyp. 2) characterized by linear viscoelastic (EL) and non linear viscoelastic (NLE) soil behavior. The white cross marks the location of the absolute maximum.

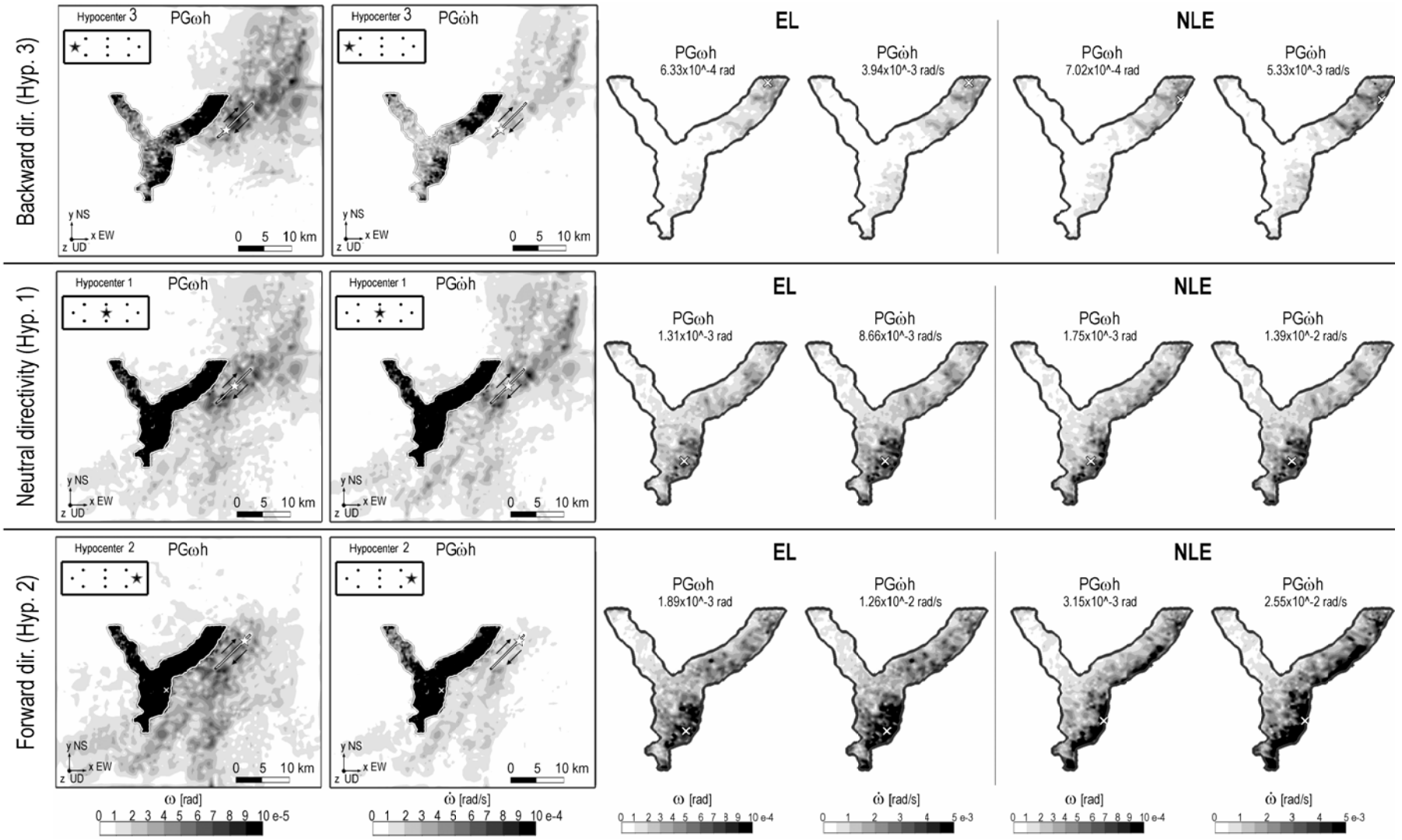

Figure 7. Similarly to Fig. 6 with maps of $PG\omega_h$ and $PG\dot{\omega}_h$

Synthetic ratios between translational and rotational peak values

In the present Section we explore to what extent rotational and translational motions are correlated, in particular we address the question of whether we can have a reasonable estimate of peak rotational motion from the corresponding translational motion studies in near source regions. In this contribution we rely on simplified models (see e.g. Igel et al., 2005 and 2007; Cochard et al. 2006) which assume an incident transversally polarized plane wave, for example along the y axis. This implies that the displacement can be described as $\underline{u} = \left[0, u_y(t - x/V_a), 0\right]$, being V_a the horizontal phase velocity. Under this assumption, at any time, transverse acceleration and rotation rate, or equivalently velocity and rotation, are in phase and the amplitudes are related by:

$$\dot{u}_y(\underline{x},t) / \omega_z(\underline{x},t) = -2V_a \qquad (7)$$

The assumption of plane wave incidence is expected to hold for a considerable part of the observed ground motion whenever the epicentral distance is large compared to the considered wavelengths and source dimensions (Igel et al., 2005). In the near field region the hypothesis of plane wave is no longer valid and a larger variability of the ratio can be expected.

Nevertheless Wang et al. (2008) showed that the ratio between peak ground acceleration and rotation rate ($PGA_h(\underline{x}) / PG\dot{\omega}_z(\underline{x}) = 2c_s$), equivalent to rotation (Eq. 1), could provide important information regarding the basin structure even in the near field. Wang et al. (2008) analyzed a hypothetical M_W=7.0 strike-slip event occurring along the Newport-Inglewood fault embedded in the 3D Los Angeles basin, and showed that high values of c_s are located outside the basin and low values inside. The only exception to the proportionality between translational and rotational motion happens in the region around the fault, where the c_s value could be used to constrain the rupture process (Takeo and Ito, 1997; Takeo, 1998). In the following we present map of the ratio between peak ground velocity and rotation.

The quantity V_a in Eq. 7 is related to the shear propagation velocity present at location $\underline{x}$, being equal to the S-wave velocity for infinite media or to the apparent wave propagation velocity if $\underline{x}$ is at the surface of a half space. On the other hand, the quantity c_s in Eq. 1 is the scaling factor between translational and rotational peak ground motions as estimated by either empirical or numerical data. Under the assumption that *SH* and *Love* waves are the predominant contributions,

which seems a reasonable approximation in the proximity of shallow strike-slip events, as in Grenoble case, Eq. 1 provides a simplified approach for evaluating V_a .

Applying Eq. 1 to the set of 14400 6-component synthetic seismograms at the Grenoble basin and surrounding we obtain the map of the value of c_s at the model's surface. The results are plotted in Figure 8a, where we can see how the basin is clearly distinguishable from the surrounding bedrock. Recall that the basin has S-wave velocities varying with depth according to Eq. 4, whereas the bedrock is a homogeneous material with 3200m/s S-wave velocity. Additionally, we can compare our obtained c_s map with the depth basin map (Figure 8b) and we observe a strong correlation. In particular, the shallower regions of the southern end of the basin, with depths 100m or less, are clearly highlighted in the c_s map. This correlation is due to both, the S-wave velocity depth dependence in our case study and the depth structure sensitivity characteristic of surface waves. Furthermore, on the bedrock, some observed features correlate well with the topography, especially the valleys between the two northern spikes of the Y-shaped basin. This suggests a possible important effect of the topography on the rotational wave field. A further remarkable area is the fault itself, whose rupture plane is clearly observable due to the small horizontal surface velocity recorded right above the fault.

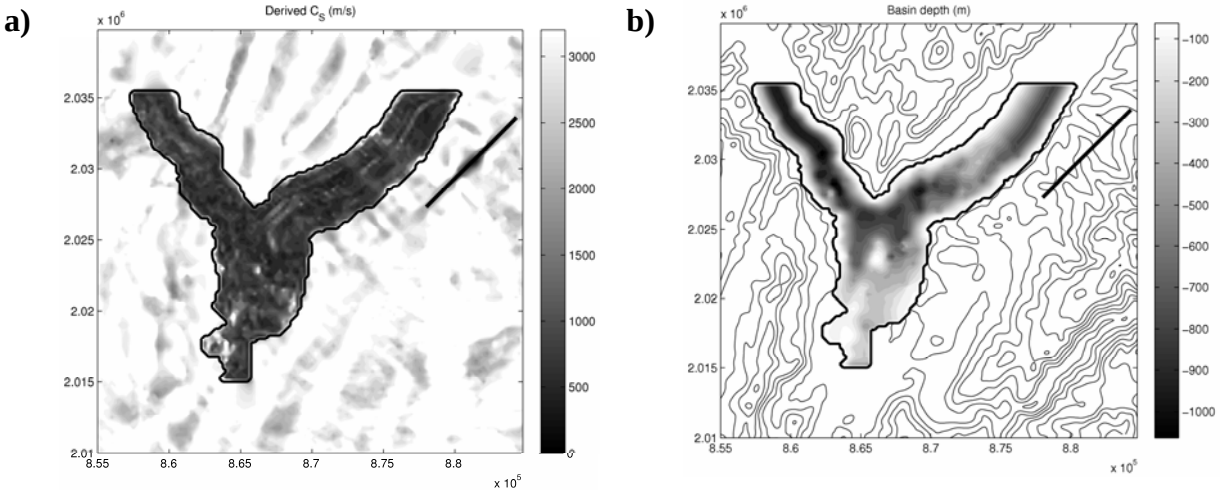

Figure 8. a) Estimated apparent velocity obtained from $PGV_h(\underline{x})/PG\omega_z(\underline{x})$ ratios. b) Grenoble basin's depth and the topography.

Comparison between Grenoble synthetics and data of past studies

Adopting Eq. 1 we study the relation between rotational and translational motion for a collection of data which must be discussed carefully due to their different origins and qualities. We can basically divide the data in three distinct subgroups. The first are peak rotational and translational values obtained in past studies, mainly those labeled 1 to 16 in Table I, for which we do not possess the whole time histories. A second data subgroup are field recordings, array derived, for which detailed information is available. Those are labeled 17 to 24 in Table I. In particular, 17 to 20 are data obtained by Paolucci & Smerzini (2008) through an empirical procedure based on a suitable spatial interpolation technique of displacement recordings from dense arrays at Parkway Valley, New Zealand (points 16 and 17) and UPSAR, California (points 18 and 19). For the data values 17 to 20 we plot the average value (filled circle) and their minimum and maximum value (denoted by bars). Also the estimates recently derived by Spudich & Fletcher (2008) for the 2004 M_w=6.0 Parkfield event and three aftershocks (in order of decreasing magnitude, M_w=5.1, M_w=4.9 and M_w=4.7), labelled from 21 to 24 in Table I, are used. In this case the authors applied the so-called "seismo-geodetic" approach to the UPSAR recordings in order to derive tilts and torsions. Referring to Spudich & Fletcher (2008), we considered three sub-array estimates for each event, filtered in the frequency band between 0.1 and 1.4 Hz (points from 21 to 24) for comparison purposes with the SE synthetics with a maximum frequency of 2 Hz. The third and last data subgroup is the synthetics obtained for the numerical study of the Grenoble valley, for M_w=6.0 and M_w=4.5 scenarios, subdivided into records obtained at the outcropping bedrock and inside the alluvial basin. All synthetics used are computed for the case of neutral directivity and viscoelastic soil behavior.

The complete dataset is presented in Figure 9. Although the comparison is not straightforward as we are combining a wide range of magnitudes, epicentral distances and sources of data, when attention focuses on the synthetic PGV_h-$PG\omega_z$ pairs, some interesting features can be noted. Primarily, the synthetic data, subdivided into alluvial and bedrock conditions, suggest a linear trend between PGV_h and $PG\omega_z$ in log-log space. In order to have a quantitative estimate of such a tendency, we decided to fit the synthetic data by a least squares linear regression. The best-fitted lines turn out to be:

$$Log_{10}PG\omega_z = Log_{10}PGV_h - 3.96 \quad \text{at outcropping bedrock,} \quad (8)$$

$$Log_{10}PG\omega_z = Log_{10}PGV_h - 3.34 \quad \text{in the alluvial basin.} \qquad (9)$$

It is remarkable that the coefficient of proportionality of both Eq. 8 and 9 is naturally very close to 1, suggesting a linear relationship between PGV_h and $PG\omega_z$, in agreement with Eq. 1, at least for the considered range of frequencies (0.1-2.0Hz). Specifically, two straight lines, superimposed in Figure 9, with $c_S \sim$ 4500m/s (thick line) and $c_S \sim$1000 m/s (thin line) describe with reasonable accuracy the $PG\omega_z$ values obtained at the outcropping bedrock and on the basin, respectively, for both the M_w=4.5 and M_w=6 earthquake scenarios. If, on one side, synthetic data show a linear trend regardless of magnitude, the dependence on site effects turns out to be pronounced. Passing from soft alluvial conditions to outcropping bedrock, the PGV_h / $PG\omega_z$, ratio increases by a factor of about 4, in average.

Nevertheless, it should be noted that the interpretation of c_S as the actual apparent propagation velocity V_a might be misleading. As also commented by Spudich & Fletcher (2008), c_S can be reasonably regarded as a scaling factor between peak rotations and translations rather than a true phase velocity at the selected model.

The array-derived estimates retrieved by Paolucci & Smerzini (2008) (points from 17 to 20) show very similar values and trend with respect to the synthetics. Their behavior alone is also remarkably linear leading to $c_S \sim$ 1000 m/s, irrespectively of the different site conditions. As a matter of fact, while points 17 and 18 fit fairly well with the synthetics calculated in the soft alluvial basin, points 19 and 20, which correspond more to bedrock conditions, seem not to be consistent with the ratio $c_S \sim$ 4500 m/s as inferred from the numerical simulations. The sub-array estimates of Spudich & Fletcher (2008) (see points from 21 to 24) are consistent with synthetics, provided the relatively stiff conditions of the UPSAR.

The single available direct measurement of the ratio $PGV_h / PG\omega_z$ seems to be significantly larger than all the simulated and array-derived estimates (point 13). However, this data refers to an explosion rather than an earthquake, so that the comparison may be improper. Unfortunately, the measurements from Takeo (1998) can not be used on the present study, since only rotation rates records of the M_w~5.0 Ito-Japan events, are available. Nevertheless, also Spudich & Fletcher (2008) commented a substantial disagreement between Takeo's measurements and empirical estimates for the reasons shortly illustrated previously. Thus, his direct measurements of rotation rates turns out to be larger, by factor of 5-60, than other estimates and the ratio of $PGV_h / PG\omega_z$ is systemically higher than those of Parkfield and Chi-Chi earthquakes (see Spudich & Fletcher 2008).

At this point we can try to answer whether or not we can infer $PG\omega_z$ from PGV_h. As a first approximation, it is clear that an average trend exists, mainly following Eq. 1, which allows for a rough estimation of the average rotational peak values given a suitable measure of the phase velocity at the receiver site. This might be helpful for quick estimates, although Figure 8 shows us the large variability displayed in the Grenoble area. This indicates that average values only are not sufficient to explain the complex behavior of rotational ground motions at the surface. More detailed pictures of rotational energy distribution should be obtained, preferably by deploying rotational sensors or seismometer arrays, in order to further identify more complex factors not only related to the local phase velocity but to other factors as topography, spatial incoherence or source-related effects.

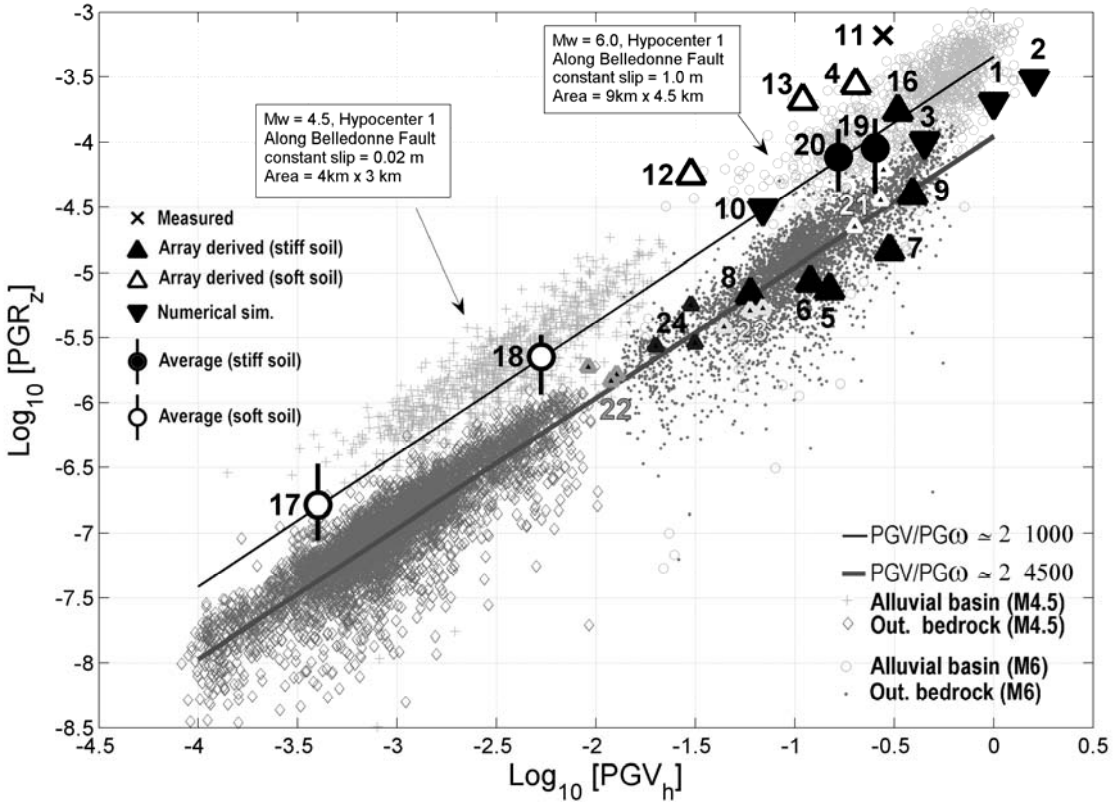

Figure 9 – Synthetic values of Peak Ground horizontal Velocity (PGV_h) vs. Peak Ground Rotation ($PG\omega_z$) in logarithmic scale obtained with M_W=6.0 and M_W=4.5, neutral directivity and linear viscoelastic soil behavior. Superimposed are the individual data retrieved from literature, listed in Table I. Data from 18 to 21 are plotted in terms of average value (filled circle) and their minimum and maximum value (denoted by bars).

Conclusions

In this paper we show a selection of available data concerning observed and synthetic rotational motion mainly regarding near field and strong motion earthquakes. The lack of observation testifies the need to investigate more carefully the role of rotations, almost neglected in seismological and hazard assessment studies. Using two well-established and accurately validated numerical techniques (SEM, ADER-DG) we simulated the rotational wavefield induced by a M_W=6.0 and a M_W=4.5 earthquake, occurring in the valley of Grenoble (French alps). The expected peak ground rotation ($PG\omega$) values on receivers located on soft soil is roughly 1 mrad and the peak ground rotation rate ($PG\dot{\omega}$) 10 mrad/s. Those values show a strong dependence on the hypocenter location, the radiation pattern and directivity effect, local site conditions and topographical features, inducing a variability of almost one order of magnitude in a range of distances of 20 km.

Numerical simulations show also a general trend correlating the maximum of rotational and translational motion. As a first approximation the estimate of $PG\omega_z$ can be regarded as linearly proportional to PGV_h, being the proportionality related to the mechanical properties of the medium around the receivers. Furthermore, this observation seems to be relatively independent of the magnitude of the earthquake. However, the overall collection of PGV_h - $PG\omega_z$ pairs shows a large variability of up to 2 orders of magnitude around the average trend. This latter observation testifies that, at least in the near field, we must treat the rotational wavefield as independent from translation.

Concluding, we remark the need of records of rotational components of the seismic wavefield coupled with classical translational motions, which can be achieved only with rotational sensors specifically designed. Only this kind of records could in the future assess a definitive answer to the relationship between velocity and rotation, and offer a set of data capable to explain the large variability that rotations seem to show.

Acknowledgments

This work enjoyed the cooperation of many individuals and institutions during its different stages. We deeply thank CRS4, and in particular F. Maggio and L. Massidda, for the essential cooperation in the development of GeoELSE; L. Scandella for collaborating to develop the subroutines for nonlinear elastic soil behaviour; E. Chaljub for organizing the Grenoble benchmark and providing the necessary information for constructing and processing the numerical model; E. Faccioli for his continuing support since the early stage of development of GeoELSE. The cooperation of the Leibniz Rechenzentrum in Muenchen, for providing their supercomputing facilities, and of P. Bunge for allowing the extensive use of the Tethys cluster is also gratefully acknowledged. This work has been financially supported by the Marie-Curie Training Network SPICE (Seismic Wave Propagation and Imaging in Complex Media).

References

Bodin, P., J. Gomberg, S. K. Singh, and M. Santoyo (1997). Dynamic deformations of shallow sediments in the Valley of Mexico, Part I: Three-dimensional strains and rotations recorded on a seismic array, Bull. Seism. Soc. Am., 87, 528 - 539.

Bouchon, M., and K. Aki (1982). Strain, tilt, and rotation associated with strong ground motion in the vicinity of earthquake faults, Bull. Seism. Soc. Am., 72, 1717-1738.

Castellani, A., and Boffi, G. (1986). "Rotational components of the surface ground motion during an earthquake." Earthquake Eng. Struct. Dyn., 14,5, 751–767.

Chaljub E. (2006). Numerical Benchmark of 3D Ground Motion Simulation in the Valley of Grenoble, French Alps, http://esg2006.obs.ujf-grenoble.fr/BENCH2/benchmark.html.

Cochard A., H. Igel, A. Flaws, B. Schuberth, J. Wassermann, W. Suryanto (2006) Rotational motions in seismology: theory, observation, simulation, in Earthquake source asymmetry, structural media and rotation effects , eds. Teisseyre et al., Springer Verlag

Day, S.M., R. Graves, J. Bielak, D. Dreger, S. Larsen, K.B. Olsen, A. Pitarka and L. Ramirez-Guzman (2007). Model for Basin Effects on Long-Period Response Spectra in Southern California, Earthquake Spectra, in press.

Dumbser, M. and M. Käser (2006). An arbitrary high order discontinuous Galerkin method for elastic waves on unstructured meshes II: the three-dimensional isotropic case, *Geophys. J. Int.,* 167, 319–336.

Faccioli E, F. Maggio, R. Paolucci, A. Quarteroni (1997). 2D and 3D elastic wave propagation by a pseudo-spectral domain decomposition method. Journal of Seismology, 1, 237-251.

Fichtner, A. and H. Igel (2008). Sensitivity densities for rotational ground motion measurements, *submitted to BSSA*.

Ghayamghamian M. R. and G. R. Nouri, 2007, On the characteristics of ground motion rotational components using Chiba dense array data, Earthquake Engng Struct. Dyn. 2007; 36:1407–1429, DOI: 10.1002/eqe.687

Graizer, V. M. (1989). “Bearing on the problem of inertial seismometry.” Izv., Acad. Sci., USSR, Phys. Solid Earth, 25, 1, 26–29.

Graizer, V. M. (2005). “Effect of tilt on ground motion data processing.” Soil Dyn. Earthquake Eng., 25,3, 197–204.

Graizer, V. M. (2006a). “Equation of pendulum motion including rotation sand its implications to the strong-ground motion.” Earthquake source asymmetry, structural media, and rotation effects, Monograph, 471–491.

Graizer, V. M. (2006b). “Tilts in strong ground motion.” Bull. Seismol. Soc. Am., 96,6, 2090–2102.

Huang, B.-S. (2003). Ground rotational motions of the 1999 Chi-Chi, Taiwan, earthquake as inferred from dense array observations, Geophys. Res. Let., 30, 40-1 - 40-4, doi: 10.1029/2002GL015157.

Igel H, Schreiber U, Flaws A, Schuberth B, Velikoseltsev A, Cochard A. (2005) Rotational motions induced by the M 8.1 Tokachi-oki earthquake, September 25, 2003. Geophysical Research Letters 2005; 32:L08309. doi: 10.1029/2004GL022336

Igel, H., A. Cochard, J. Wassermann, A. Flaws, U. Schreiber, A. Velikoseltsev, and N. Dinh (2007). Broad-band observations of earthquake-induced rotational ground motions, Geophys. J. Int., 168, 182-196, doi: 10.1111/j.1365-246X.2006.03146.x.

Jerram J., P. Foray, S. Labanieh, E. Flavigny (2006). Characterising the non linearities of lacustrine clays in the Grenoble basin, Proc. 3rd Int. Symp. on the Effects of Surface Geology on Seismic Motion (ESG), Grenoble, France.

Kalkan E, Graizer V. (2007) Coupled tilt and translational ground motion response spectra. ASCE J Struct Eng; 133(5):609–19.

Käser, M. and M. Dumbser (2006). An arbitrary high-order discontinuous Galerkin method for elastic waves on unstructured meshes – I. The two-dimensional isotropic case with external source terms, *Geophys. J. Int.*, 166, 855–877.

Käser, M., M. Dumbser and J. de la Puente (2006). An efficient ADER-DG method for 3-Dimensional seismic wave propagation in media with complex geometry, *in Proceedings of ESG 2006, Third International Symposium on the Effects of Surface Geology on Seismic Motion*, Laboratoire Central des Ponts et Chausses. 1, 455–464.

Komatitsch D. and J.P. Vilotte (1998). The spectral element method: an efficient tool to simulate the seismic response of 2D and 3D geological structures. Bull. Seism. Soc. Am., 88, 368-392.

Kramer, S.L. (1996). Geotechnical Earthquake Engineering, Prentice Hall, Inc., Upper Saddle River, New Jersey

Lee, V. W., and Trifunac, M. D. (1985). "Torsional accelerograms." Soil Dyn. Earthquake Eng., 4,3, 132–142.

McLeod, D.P., Stedman, G.E., Webb, T.H. & Schreiber, U., 1998. Comparison of standard and ring laser rotational seismograms, Bull. seism. Soc. Am., 88, 1495–1503.

Newmark, N.M., 1969. Torsion in symmetrical buildings. Proc. Fourth World Conference on Earthquake Engineering, Santiago, Chile, 3, 19-32.

Niazi, M. (1986). "Inferred displacements, velocities and rotations of a long rigid foundation located at El Centro differential array site during the 1979 Imperial Valley, California earthquake." Earthquake Eng. Struct. Dyn., 14,4, 531–542.

Nigbor, R. L. (1994). "Six-degree of freedom ground motion measurement." Bull. Seismol. Soc. Am., 84,4, 1665–1669.

Oeser, J., H.-P. Bunge, and M. Mohr (2006), Cluster Design in the Earth Sciences: TETHYS, in High Performance Computing and Communications - Second International Conference, HPCC 2006, Munich, Germany, Lecture Notes in Computer Science, vol. 4208, edited by Michael Gerndt and Dieter Kranzlmüller, pp. 31-40, Springer, doi:10.1007/11847366_4.

Oliveira, C.S., and B.A. Bolt (1989). Rotational components of surface strong ground motion, Earthq. Eng. Struct. Dyn., 18, 517-526.

Paolucci R. and Smerzini C.,"Earthquake-induced transient ground strains from dense seismic networks", submitted to Earthquake Spectra

Pancha, A., Webb, T.H., Stedman, G.E., McLeod, D.P. & Schreiber, K.U., 2000. Ring laser detection of rotations from teleseismic waves, Geophys. Res. Let., 27, 3553–3556.

Pillet, R. and J. Virieux, The effects of seismic rotations on inertial sensors, Geophys. J. Int., (2007) 171, 1314–1323, doi: 10.1111/j.1365-246X.2007.03617.x

Richter, C. F. (1958). Elementary Seismology, W. H. Freeman, San Francisco, 129-132.

Singh, S.K., Santoyo, M., Bodin, P.&Gomberg, J., 1997. Dynamic deformations of shallow sediments in the Valley of Mexico, part ii: single-station estimates, Bull. seism. Soc. Am., 87, 540–550.

Spudich, P., L.K Steck, M. Hellweg, J. Fletcher, and L.M. Baker (1995). Transient stresses at Parkfield, California, produced by the M7.4 Landers earthquake of June 28, 1992: observations from the UPSAR dense seismograph array, J. Geophys. Res. 100, 675-690.

Spudich, P., and J. Fletcher (2008). Observation and prediction of dynamic ground strains, tilts and torsions caused by the M6.0 2004 Parkfield, California, earthquake and aftershocks derived from UPSAR array observations, accepted to BSSA

Which one???

Stedman G.E. , Z. Li, C.H. Rowe, A.D. McGregor, H.R. Bilger. Harmonic analysis in a large ring laser with backscatter-induced pulling. In Physical Review A, 51 (6): 4944--4958, 1995.

Stedman GE, Li Z, Bilger HR. Side band analysis and seismic detection in a large ring laser. Applied Optics 1995; 34:7390–7396.

Stratta, J. L., and Griswold, T. F. (1976). Rotation of footing due to surface waves. Bull. Seismol. Soc. Am., 66 1, 105–108.

Stupazzini M. (2004) A spectral element approach for 3D dynamic soil-structure interaction problems. Ph.D. thesis Politecnico di Milano, Italy.

Stupazzini M., Paolucci R., Igel H. (2008), "Near-fault earthquake ground motion simulation in the Grenoble Valley by a high-performance spectral element code", submitted to BSSA

Suryanto, W., H. Igel, J. Wassermann, A. Cochard, B. Schuberth, D. Vollmer, F. Scherbaum, U. Schreiber, and A. Velikoseltsev (2006). First comparison of array-derived rotational ground motions with direct ring laser measurements, Bull. Seism. Soc. Am., 96, 2059-2071, doi: 10.1785/0120060004.

Takeo, M. and H.M. Ito (1997). What can be learned from rotational motions excited by earthquakes, Geophys. J. Int., 129, 319-329.

Takeo, M. (1998). Ground rotational motions recorded in the near-source region of earthquakes, Geophys. Res. Let., 25, 789-792.

Trifunac, M.D. (1982). A note on rotational components of earthquake motions for incident body waves, Int. J. Soil Dynamics and Earthquake Engineering, 1, 11-19.

Trifunac, M. D., and Todorovska, M. I. (2001). "A note on the usable dynamic range of accelerographs recording translation." Soil Dyn. Earthquake Eng., 21,4, 275–286.

Wang H., Igel H., Gallovic F. and A. Cochard (2008), Source and basin effects on rotational ground motions: comparison with translations, submitted for publications to BSSA

AUTHORs AFFILIATIONS

[1]Department of Structural Engineering, Politecnico di Milano
P.zza Leonardo da Vinci 32, 20133, Milano, Italy

[2] Department für Geo- und Umweltwissenschaften Sektion Geophysik, Ludwig-Maximilians Universität, Theresienstrasse 41, 80333, München, Germany

TABLES

Table I. XXX.